# Evidence for Quantum Critical Behavior in the Optimally Doped Cuprate $Bi_2Sr_2CaCu_2O_{8+\delta}$

T. Valla *et al.*

*Science* **285**, 2110 (1999);
DOI: 10.1126/science.285.5436.2110

Si dimers on Si(100) (*18*). Inoue *et al.* have mapped the Si(100) surface onto a two-dimensional Ising Hamiltonian in a random magnetic field (to simulate defect pinning) and performed Monte Carlo simulations to model its thermodynamic behavior (*19*). They showed that the anticipated second-order phase transition in Si(100) is smeared out by defects. Our observations are consistent with their analysis. A difference from the Si(100) scenario is that the triangular Sn/Ge(111) system with static disorder should be mapped onto the random-field three-state Potts model rather than onto an Ising model (*20*). Most importantly, however, the substitutional disorder in these triangular lattice systems is neither static nor completely random, as is the case in the random-field model of statistical physics. Because the effects of quenched randomness are especially profound when $d \leq 2$, it would be interesting to explore when and how the defect degrees of freedom alter the conclusions of the random-field model.


**References and Notes**

1. G. Grüner, *Density Waves in Solids* (Addison-Wesley, Reading, MA, ed. 1, 1994).
2. J. A. Wilson, F. J. DiSalvo, S. Mahajan, *Adv. Phys.* **24**, 117 (1975).
3. Y. Imry and S.-K. Ma, *Phys. Rev. Lett.* **35**, 1399 (1975).
4. D. S. Fisher, G. M. Grinstein, A. Khurana, *Phys. Today* **41**, 56 (December 1988).
5. M. Aizenman and J. Wehr, *Phys. Rev. Lett.* **62**, 2503 (1989).
6. K. Hui and A. N. Berker, *ibid.*, p. 2507.
7. J. Cardy, *Physica A* **263**, 215 (1999).
8. X. L. Wu and C. M. Lieber, *Phys. Rev. B* **41**, 1239 (1990); B. Giambattista, C. G. Slough, W. W. McNairy, R. V. Coleman, *ibid.*, p. 10082.
9. J. M. Carpinelli, H. H. Weitering, R. Stumpf, E. W. Plummer, *Nature* **381**, 398 (1996).
10. J. M. Carpinelli, H. H. Weitering, M. Bartkowiak, R. Stumpf, E. W. Plummer, *Phys. Rev. Lett.* **79**, 2859 (1997).
11. J. J. Metois and G. Le Lay, *Surf. Sci.* **133**, 422 (1983).
12. J. M. Carpinelli, H. H. Weitering, E. W. Plummer, *ibid.* **401**, L457 (1998).
13. R. Stumpf, J. M. Carpinelli, H. H. Weitering, *Phys. Rev. B* **59**, 15779 (1999).
14. A. V. Melechko, J. Braun, H. H. Weitering, E. W. Plummer, in preparation.
15. J. Dumas, A. Arbaoui, H. Guyot, J. Marcus, C. Schlenker, *Phys. Rev. B* **30**, 2249 (1984).
16. D. Weaire and N. Rivier, *Contemp. Phys.* **25**, 59 (1984); M. Bartkowiak, unpublished material.
17. J. Avila *et al.*, *Phys. Rev. Lett.* **82**, 442 (1999).
18. P. C. Weakliem, G. W. Smith, E. A. Carter, *Surf. Sci.* **232**, L219 (1990).
19. K. Inoue, Y. Morikawa, K. Terakura, M. Nakayama, *Phys. Rev. B* **49**, 14774 (1994).
20. S. Alexander, *Phys. Lett. A* **54**, 353 (1975); M. Schick, J. S. Walter, M. Wortis, *Phys. Rev. B* **16**, 2205 (1977). A possible first-order transition would also be preempted by random defects as discussed in (*5*–*7*).


21. We thank T. Einstein, T. Lubensky, and K. Terakura for enlightening discussions. This work was supported by the NSF under grants NSF-DMR 9705246 (H.H.W.) and NSF-DMR 9801830 (E.W.P.). Oak Ridge National Laboratory is managed by Lockheed Martin Energy Research Corporation for the U.S. Department of Energy under contract DE-AC05-96OR22464.

9 June 1999; accepted 11 August 1999


# Evidence for Quantum Critical Behavior in the Optimally Doped Cuprate $Bi_2Sr_2CaCu_2O_{8+\delta}$


**T. Valla,[1] A. V. Fedorov,[1] P. D. Johnson,[1] B. O. Wells,[1,4] S. L. Hulbert,[2] Q. Li,[3] G. D. Gu,[5] N. Koshizuka[6]**



**The photoemission line shapes of the optimally doped cuprate $Bi_2Sr_2CaCu_2O_{8+\delta}$ were studied in the direction of a node in the superconducting order parameter by means of very high resolution photoemission spectroscopy. The peak width or inverse lifetime of the excitation displays a linear temperature dependence, independent of binding energy, for small energies, and a linear energy dependence, independent of temperature, for large binding energies. This behavior is unaffected by the superconducting transition, which is an indication that the nodal states play no role in the superconductivity. Temperature-dependent scaling suggests that the system displays quantum critical behavior.**


Understanding transport in the cuprate superconductors and other synthetic metals is at the heart of current research in solid-state physics. There is speculation that the elementary excitations in these materials might well be drastically different from those in traditional metals where Fermi liquid theory has proved most successful (*1*). Angle-resolved photoemission (ARPES) has been an important experimental probe of the electronic excitations, providing insight into the fundamental interactions and quantities, such as the single-particle self energy $\Sigma$. The self energy reflects the interaction of the excitation with its local environment: the real part describing the screening of the excitation and the imaginary part describing the inverse lifetime. These microscopic properties are reflected in macroscopic behavior such as conductivity and the optical response. In two-dimensional (2D) systems, the self-energy effects measured in photoemission reflect solely the response to the photohole created in the emission process. As such, ARPES has provided a number of important insights into the cuprates, where the superconductivity is believed to be associated with the 2D $CuO_2$ planes. Highlights from ARPES include mapping of the Fermi surface (*2*), the identification of d-wave symmetry of the order parameter in the superconducting state (*3*), and the detection of a pseudogap for underdoped compounds above the transition temperature $T_c$ (*4, 5*). However, the limited energy and momentum resolution of ARPES to date have meant that a quantitative determination of the $\Sigma$ underlying the ARPES spectra has remained a considerable challenge.

Here we present ARPES data obtained from optimally doped $Bi_2Sr_2CaCu_2O_{8+\delta}$, with excellent energy and momentum resolution, and employ a method of analysis allowing a detailed evaluation of the self energy along the $(0,0) \rightarrow (\pi,\pi)$ direction as a function of both binding energy and temperature. Overall, the imaginary component of $\Sigma$ measured here is very different from that expected for a Fermi liquid or indeed that measured in normal metals (*6*). In the former, the width or scattering rate as determined by electron-electron interactions should have an $\omega^2$ and $T^2$ dependence (where $\omega$ is the binding energy). In most metals, the electron-phonon interaction dominates. The self energy due to this interaction displays a rapid change in the scattering rate in the vicinity of the Fermi level and saturation at higher energies (*7*). However, in the present study of a high-temperature superconductor, we find possible evidence for quantum critical behavior. The possibility of such behavior has recently been discussed in several models of high-$T_c$ superconductivity (*8*). In a quantum critical system, a phase transition can occur at zero temperature. As such, the transition is driven by quantum fluctuations rather than thermal fluctuations.

The present measurement can also be tied to conductivity measurements of the bulk material. Transport indicates that for optimally doped compounds, the resistivity in the normal state, and thus the inverse lifetime at the Fermi level, is linear with temperature over a wide range (*9*). Furthermore, infrared studies indicate that the scattering rate is linear in both temperature and frequency (*10*).

The photoemitted intensity in the $(0,0) \rightarrow (\pi, \pi)$ direction of the Brillouin zone (Fig. 1), as indicated by the arrow in the upper left inset, represents a 2D intensity map with binding energy in one dimension and momentum in the


[1]Department of Physics, [2]National Synchrotron Light Source, [3]Division of Materials Sciences, Brookhaven National Laboratory, Upton, NY 11973–5000, USA. [4]Department of Physics, University of Connecticut, Storrs, CT 06269, USA. [5]School of Physics, The University of New South Wales, Post Office Box 1, Kensington, New South Wales, Australia 2033. [6]Superconductivity Research Laboratory, ISTEC, 10-13, Shinonome I-chrome, Koto-ku, Tokyo 135, Japan.

other (*11*). The intensity at any point is given by a false color scale, with white being the most intense. The two other insets show 1D scans obtained by taking cross-section cuts through the data in orthogonal directions. The lower right inset shows a cross section of the intensity as a function of energy at a constant in-plane momentum. Such a scan represents an energy distribution curve (EDC), which is the standard format for acquiring and displaying photoemission data. The inset in the upper right is an alternative method of displaying ARPES information. It shows the intensity as a function of parallel momentum at constant energy—a momentum distribution curve (MDC).

The 2D intensity plot $I(\mathbf{k},\omega)$ represents a direct visualization of the spectral function of the photohole, $A(\mathbf{k},\omega)$, weighted by the Fermi distribution function. $A(\mathbf{k},\omega)$ is given by (*12*)

$$A(\mathbf{k},\omega) \propto \frac{1}{\pi} \frac{\mathrm{Im}\Sigma(\mathbf{k},\omega)}{[\omega - \varepsilon_k - \mathrm{Re}\Sigma(\mathbf{k},\omega)]^2 + [\mathrm{Im}\Sigma(\mathbf{k},\omega)]^2} \quad (1)$$

where $\mathrm{Re}\Sigma(\mathbf{k},\omega)$ and $\mathrm{Im}\Sigma(\mathbf{k},\omega)$ represent the real and imaginary components of the self energy, respectively. The width of the photoemission peak in an EDC reflects the inverse lifetime, $\hbar/\tau$ and is given by $|2\mathrm{Im}\Sigma(\mathbf{k},\omega)|$. Similarly, the width of the peak in an MDC reflects the mean free path $\ell = 1/\Delta k$ such that

$$\hbar v_k \Delta k = \frac{\hbar v_k}{\ell} \approx |2\mathrm{Im}\Sigma(\mathbf{k},\omega)| \quad (2)$$

Here $v_k$ represents the velocity of the excitation as determined by the band dispersion. Previous work analyzing ARPES line shapes from the cuprates concentrated on EDCs and attempted to fit the line shape to some form of $A(\mathbf{k},\omega)$. Several difficulties arise with this procedure. In any EDC, there is a background component that is not included within $A(\mathbf{k},\omega)$. Determining which fraction should be regarded as this component is not straightforward. Furthermore, the line shapes of EDCs in these materials are complex, with no unique theoretical description to serve as a guide. The use of MDCs has several benefits. At the Fermi level, the peaks are symmetric with a simple background. Away from the Fermi level, the peaks develop a slight asymmetry reflecting the binding energy dependence of ImΣ. Ambiguities are not introduced by the Fermi function cutoff. The background in a MDC is constant because the step-like distribution in the vicinity of the Fermi level, which appears to exist at all momenta, is sampled at a constant energy. Finally, it is possible to take MDC cuts that are closely spaced in energy. These combined advantages allow an easier determination of the positions and widths of peaks. The resulting dispersion obtained from such cuts is more detailed than, but in general agreement with, previously published results. In agreement with calculation (*13*), the wave vector corresponding to the Fermi surface crossing is equal to 0.446 $\text{Å}^{-1}$ or 0.391(π,π). In addition, the velocity or rate of dispersion changes in the vicinity of the Fermi level, resulting in an increased effective mass $m^*$ such that $m^*/m_b \approx 1.6$, where $m_b$ represents the mass at higher binding energies.

The MDCs taken at $\omega = 0.0 \pm 2.5$ meV for several temperatures (Fig. 2A) represent the ARPES intensity at $E_F$ as a function of momentum along the (0,0) → (π,π) direction. Fitting the scans with a Lorentzian, we obtain momentum widths $\Delta k$ for several samples over a range of temperatures (Fig. 2B). The offset between the different sets of data represents a small broadening, which varies from one cleave to another. However, the slopes are all identical within error bars. Also

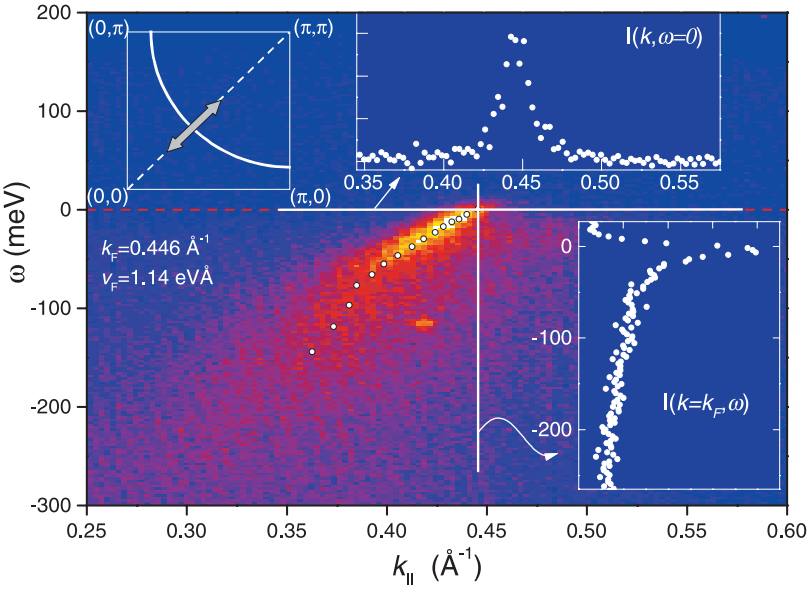


**Fig. 1.** Two-dimensional spectral plot showing the intensity of emission in the (π,π) direction of the Brillouin zone as a function of ω, the binding energy, and $k_{||}$, the parallel momentum. The photon energy is 21.2 eV and the sample temperature is 48 K. Clockwise from upper left, the insets show the region of the Brillouin zone sampled in the experiment, a cross section through the intensity at constant energy (ω = 0) as a function of momentum (an MDC), and a cross section through the intensity at constant angle or momentum ($k = k_F$) as a function of ω (an EDC).

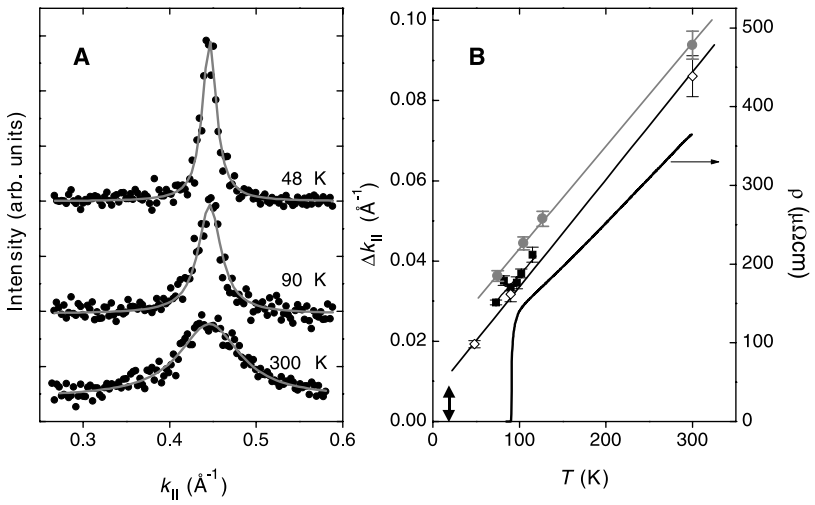


**Fig. 2.** (**A**) Momentum distribution curves as a function of temperature. The cuts are made at a binding energy corresponding to the Fermi surface. (**B**) $\Delta k_{||}$ obtained from MDCs of the type shown in (A) for three samples indicated by the circles, squares, and diamonds. The error bars represent the statistical uncertainties from the fits to Lorentzian line shapes The thin lines represent linear fits to the data. The solid black line shows the temperature dependence of the resistivity ρ measured on an identical sample. The double-headed arrow indicates the combined energy and angular contributions to the momentum resolution of the experiment.

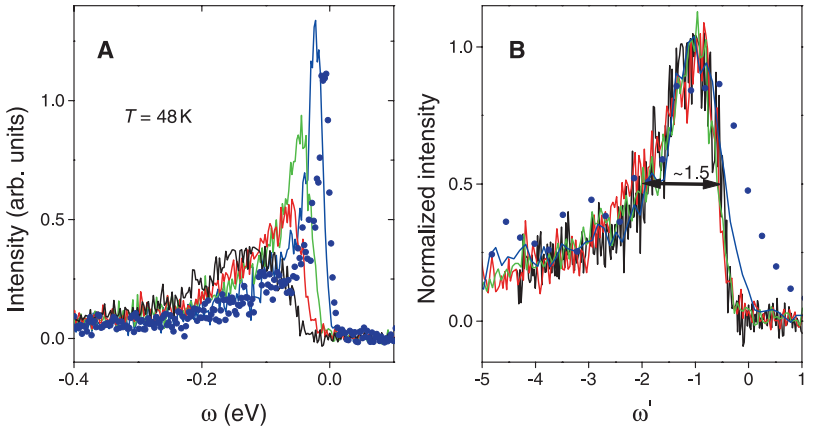


**Fig. 3.** (**A**) EDCs obtained in the (0,0) → (π,π) direction after background subtraction. (**B**) EDCs scaled to the same peak position, showing that the overall shape scales linearly with binding energy. The peak width is approximately 1.5 times the binding energy in all spectra (double-headed arrow).

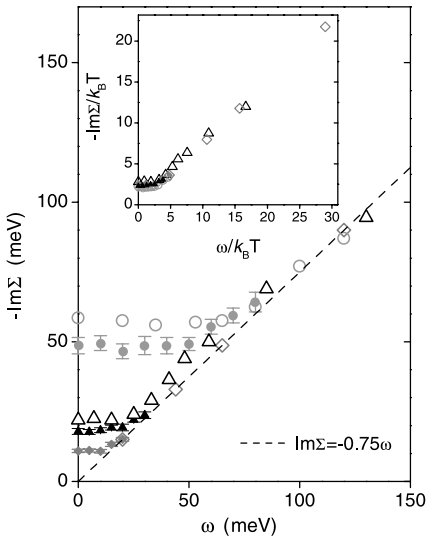


**Fig. 4.** A compilation of ImΣ obtained from Δ*k* cuts or MDCs (solid symbols) and from peak widths in EDCs (open symbols) as a function of binding energy for 48 temperatures of K (diamonds), 90 K (triangles), and 300 K (circles). The inset shows the same data plotted in dimensionless units confirming scaling behavior. Error bars indicate uncertainties from the fits of MDCs to Lorentzian line shapes.

shown is the resistivity of a sample from the same crystal growth with the superconducting transition at 91 K. In simple models of conductivity, the resistivity is proportional to the inverse lifetime, or from Eq. 2, to the inverse mean free path (*14*). Although inverse lifetimes measured in conductivity are not identical to those measured in photoemission, in most solid-state systems they are approximately the same (*15*), and we see (Fig. 2B) that a proportionality does exist between the two measurements in the normal state. This observation is surprising because our own data, as discussed below, and a preponderance of previous results have demonstrated that optimally doped cuprates are not well described by Fermi liquid theory. However, our observation can be taken as an indication that the same physical mechanisms underlie both measurements.

In the superconducting state, any such correlation disappears. There is no indication in Fig. 2B of any deviation in the linearity of the temperature dependence of the MDC peak widths at the transition temperature. Nor is any change observed in the peak dispersion near the Fermi level. It appears therefore that states in the (0,0) → (π,π) direction are not affected by the formation of the superconducting state. This is different from the behavior observed in other parts of the zone. The gap that opens at $T_c$ has its maximum value in the (π,0) direction, and in the same direction a sharp peak appears in the spectra reflecting the superconducting state (*3, 16*). Thus, the overall picture that emerges is that in the normal state the conductivity is related to the excitations probed by photoemission along (0,0) → (π,π) and that the property of the superconducting state is determined by states in the (π,0) region of the Brillouin zone.

A series of EDC cuts through the 2D data array of Fig. 1 (Fig. 3A) is presented after background subtraction. Here we follow a procedure used in our earlier study of emission in the (π,0) direction (*16*), where we subtract a representative background taken at a momentum **k** far from the region where any peak is found. Because there should nominally be no intensity at such a point, we assume that it represents an angle-independent background. In Fig. 3B, energies are rescaled so that the maximum intensity appears at the same energy for all EDCs, and the intensities are normalized to the same peak value. This procedure corresponds to a linear scaling of $\omega' = \omega/E_P$, with ω the measured binding energy and $E_P$ the position of the peak in an EDC. Despite their asymmetric shape, the EDCs at higher binding energies all scale linearly with binding energy, a direct indication that the width is proportional to ω. We also note from the scaling procedure that the width of the peak at binding energy ω is approximately 1.5 ω.

Summarizing ImΣ versus energy, data recorded at three temperatures from the same cleave along the (0,0) → (π,π) direction are shown (Fig. 4). Values derived from fits to MDC scans (converted to ImΣ using Eq. 2) are shown for the regions in which $v = v_F$. Values obtained directly from EDCs normalized to the Fermi function are also shown, along with a dashed line indicating $|\mathrm{Im}\Sigma| = 0.75\ \omega$ as determined from the scaling analysis in Fig. 3. The same behavior is obtained from analysis of either EDCs or MDCs. For a given temperature, ImΣ is constant up to some energy $\omega \sim 2.5k_BT$. At larger binding energies, ImΣ scales linearly with binding energy and is independent of temperature, which is behavior very different from that found in metallic systems (*17*). Evidence for a linear dependence of ImΣ on ω has been presented in earlier ARPES studies (*18*). The crossover energy between the two regions is temperature-dependent. This energy/temperature dependence for ImΣ, embodied in the Marginal Fermi Liquid model (MFL) (*19*) and earlier non-Fermi liquid theories (*20*) for the normal state, continues smoothly through the superconducting $T_c$. The observation that the behavior in the normal state is completely unaffected by the transition into the superconducting state suggests that the excitation is not decaying via scattering as would be the case for quasiparticles in a Fermi liquid. Such scattering would be sensitive to the change in available phase space upon formation of a gap. Rather the lack of sensitivity at $T_c$ suggests that the excitation decays through some other mechanism. The observation in the present study that the energy sets the temperature scale and the temperature sets the energy scale is consistent with quantum critical scaling (*8*). Indeed, as shown explicitly in the inset of Fig. 4, all of the data collapse onto a single curve when both ImΣ and ω are scaled by *T*, which is suggestive of quantum critical behavior. The demonstration of quantum critical behavior in the magnetic fluctuations has recently been reported in a study of the normal state of near optimally doped $La_{2-x}Sr_xCuO_4$ (*21*). The present study suggests that single particle excitations also show behavior consistent with the existence of a nearby quantum critical point and that this is in fact a general property of the cuprates. We believe that the detailed information on the **k** and ω dependence of the single-particle excitations presented here, as well as their connection to transport properties, provides both a challenge to and a constraint on any theory of these complex materials.

### References and Notes

1. P. W. Anderson, *The Theory of Superconductivity in the High-*$T_c$ *Cuprates* (Princeton Univ. Press, Princeton, NJ, 1997).
2. J. C. Campuzano *et al.*, *Phys. Rev. Lett.* **64**, 2308

(1990); D. S. Dessau *et al*., *ibid*. **71**, 2781 (1993); P. Aebi *et al*., *ibid*. **72**, 2757 (1994).
3. B. O. Wells *et al*., *Phys. Rev. B* **46**, 11830 (1992); Z.-X. Shen *et al*., *Phys. Rev. Lett*. **70**, 1553 (1993); H. Ding *et al*., *Phys. Rev. B* **54**, R9678 (1996).
4. A. G. Loeser *et al*., *Science* **273**, 325 (1996).
5. H. Ding *et al*., *Nature* **382**, 51 (1996).
6. D. Pines and P. Nozieres, *The Theory of Quantum Liquids* (Benjamin, New York, 1969).
7. G. Grimvall, *The Electron-Phonon Interaction in Metals* (North-Holland, New York, 1981).
8. S. Chakravarty, B. I. Halperin, D. R. Nelson, *Phys. Rev. B* **39**, 2344 (1989); S. Sachdev and J. Ye, *Phys. Rev. Lett.* **69**, 2411 (1992); A. Sokol and D. Pines, *ibid*. **71**, 2813 (1993); V. J. Emery and S. A. Kivelson, *ibid*., p. 3701; C. Castellani, C. Di Castro, M. Grilli, *ibid*. **75**, 4650 (1995); C. M. Varma, *Phys. Rev. B* **55**, 14554 (1997).
9. M. Gurvitch and A. T. Fiory, *Phys. Rev. Lett*. **59**, 1337 (1987).
10. A. V. Puchkov, D. N. Basov, T. Timusk, *J. Phys. Condens. Mater*. **8**, 10049 (1996).
11. The experimental studies reported here were carried out on a Scienta hemispherical analyzer. The instrument has an angular resolution of ±0.1° or better and, in the present studies, an energy resolution of ~10 meV. The total spectral response may be measured as a function of angle and energy simultaneously. Photons were provided either by a resonance lamp or by a normal incidence monochromator based at the National Synchrotron Light Source. In the photon energy range used, 15 to 21.2 eV, the angular resolution of the instrument results in a momentum resolution on the order of 0.005 $Å^{-1}$. Samples of optimally doped ($T_c$ = 91 K) $Bi_2Sr_2CaCu_2O_{8+\delta}$ produced by the floating zone method [G. D. Gu, K. Takamuku, N. Koshizuka, S. Tanaka, *J. Crystallogr. Growth* **130**, 325 (1990)] were mounted on a liquid He cryostat and cleaved in situ in the ultra-high vacuum chamber with base pressure $2 \times 10^{-9}$ Pa. During the recording of each spectrum, the temperature was measured with a silicon sensor mounted near the sample.
12. J. E. Inglesfield and E. W. Plummer in *Angle-Resolved Photoemission*, S. D. Kevan, Ed. (Elsevier, Amsterdam, 1992).
13. H. Krakauer and W. E. Pickett, *Phys. Rev. Lett*. **60**, 1665 (1988).
14. N. W. Ashcroft and N. D. Mermin, *Solid State Physics* (Saunders, Philadelphia, PA, 1976), chap. 13.
15. P. B. Allen, in *Quantum Theory of Real Materials*, J. R. Chelikowsky and S. G. Louie, Eds. (Kluwer, Boston, 1996), pp. 219–250.
16. A. V. Fedorov *et al*., *Phys. Rev. Lett*. **82**, 2179 (1999).
17. T. Valla, A. V. Fedorov, P. D. Johnson, S. L. Hulbert, *ibid*., **83**, 2085 (1999).
18. C. Olson *et al*., *Phys. Rev. B* **42**, 381 (1990).
19. C. M. Varma, P. B. Littlewood, S. Schmitt-Rink, E. Abrahams, A. E. Ruckenstein, *Phys. Rev. Lett*. **63**, 1936 (1989).
20. P. W. Anderson, in *Frontiers and Borderlines in Many-Particle Physics* (North-Holland, Amsterdam, 1987).
21. G. Aeppli *et al*., *Science* **278**, 21 (1997).
22. We thank V. J. Emery, V. N. Muthukumar, R. J. Gooding, and S. A. Kivelson for useful discussions. Supported in part by the Department of Energy under contract number DE-AC02-98CH10886 and in part by the New Energy and Industrial Technology Development Organization.

28 April 1999; accepted 18 August 1999

# Extrusion Polymerization: Catalyzed Synthesis of Crystalline Linear Polyethylene Nanofibers Within a Mesoporous Silica

**Keisuke Kageyama, Jun-ichi Tamazawa, Takuzo Aida***

**Crystalline nanofibers of linear polyethylene with an ultrahigh molecular weight (6,200,000) and a diameter of 30 to 50 nanometers were formed by the polymerization of ethylene with mesoporous silica fiber–supported titanocene, with methylalumoxane as a cocatalyst. Small-angle x-ray scattering analysis indicated that the polyethylene fibers consist predominantly of extended-chain crystals. This observation indicates a potential utility of the honeycomb-like porous framework as an extruder for nanofabrication of polymeric materials.**

Recent developments in polymerization catalysis have enabled the precise control of the primary properties of polymers such as molecular weight, co-monomer sequence, and stereo sequence (*1*). However, for polymers to be used as commodity materials, molecular orientation (crystal structure) (*2*) or morphology (*3, 4*), or both, must also be controlled. Postprocessing steps, such as extrusion or spinning, are usually required to fabricate polymeric materials that perform more elaborate functions. Some crystalline polymers with controlled morphology are already produced in nature. For example, in the biosynthesis of highly crystalline cellulose fibers by the bacterium *Acetobacter xylinum*, cellulose synthase in a cellular membrane forms fine elementary fibrils of cellulose. They are then assembled into macrofibrils and fibers by extrusion through nanopores arranged in the cellular membrane (*5*). A regular arrangement of multiple catalytic sites on mesostructured porous materials could mimic this natural system and produce crystalline polymers with a fibrous morphology (Fig. 1).

We report the production of crystalline polyethylene fibers with a diameter of 30 to 50 nm by the polymerization of ethylene with titanocene ($Cp_2Ti$, where Cp is the cyclopentadienyl ligand) supported by a fibrous mesoporous silica in conjunction with methylalumoxane (MAO) as a cocatalyst. A mesoporous silica has a honeycomb-like framework with a uniform, controllable pore diameter from 15 to 100 Å (*6*). It is made up of a hexagonal arrangement of the linear channels. Recently, a new class of mesoporous materials called mesoporous silica fiber (MSF) has been developed, consisting of uniformly sized mesopores (27 Å) arranged in a parallel direction to the fiber axis (*7*). This material can be easily prepared by a sol-gel process at a water-oil interface. We used this material as a solid support of titanocene for the polymerization of ethylene (*8, 9*).

The MSF-supported titanocene ($Cp_2Ti$-MSF) was prepared according to a modified method of Thomas and co-workers (*10*). The powder x-ray diffraction (XRD) pattern of $Cp_2Ti$-MSF showed peaks characteristic of a hexagonal symmetry with a *d* spacing of 3.8 nm (wall thickness + pore diameter). Similar to the case for MSF (*7*), transmission electron microscopy (TEM) of finely ground $Cp_2Ti$-MSF showed a clear image of regularly arranged mesoscopic pores with a diameter of 2 to 3 nm.

The polymerization of ethylene with $Cp_2Ti$-MSF in the presence of MAO gave a cocoon-like solid mass consisting of fibrous polyethylene (PE). For example, a toluene

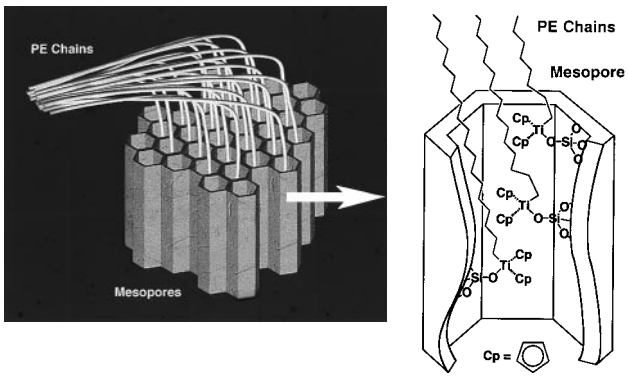


**Fig. 1.** Conceptual scheme for the growth of crystalline fibers of polyethylene by mesoporous silica–assisted extrusion polymerization.

Department of Chemistry and Biotechnology, Graduate School of Engineering, University of Tokyo, 7-3-1 Hongo, Bunkyo-ku, Tokyo 113-8656, Japan.

*To whom correspondence should be addressed. E-mail: aida@macro.t.u-tokyo.ac.jp